Intracellular Recordings of Action Potentials by an Extracellular Nanoscale Field-Effect Transistor

Share Your Story

The Harvard community has made this article openly available.
Please share how this access benefits you. Submit a story .

Accessibility

Intracellular recordings of action potentials by an extracellular nanoscale field-effect transistor

Xiaojie Duan[1], Ruixuan Gao[1], Ping Xie[1], Tzahi Cohen-Karni[2], Quan Qing[1], Hwan Sung Choe[3], Bozhi Tian[1], Xiaocheng Jiang[1], Charles M. Lieber[1,2*]

[1]Department of Chemistry and Chemical Biology, [2]School of Engineering and Applied Sciences, [3]Department of Physics, Harvard University, Cambridge, Massachusetts, 02138, USA.

[*]To whom correspondence should be addressed. E-mail: cml@cmliris.harvard.edu

The ability to make electrical measurements inside cells has led to many important advances in electrophysiology[1-6]. The patch clamp technique, in which a glass micropipette filled with electrolyte is inserted into a cell, offers both high signal-to-noise ratio and temporal resolution[1,2]. Ideally the micropipette should be as small as possible to increase the spatial resolution and reduce the invasiveness of the measurement, but the overall performance of the technique depends on the impedance of the interface between the micropipette and the cell interior[1,2], which limits how small the micropipette can be. Techniques that involve inserting metal or carbon microelectrodes into cells are subject to similar constraints[4,7-9]. Field-effect transistors (FETs) can also record electric potentials inside cells[10], and since their performance does not depend on impedance[11,12], they can be made much smaller than micropipettes and microelectrodes. Moreover, FET arrays are better suited for multiplexed measurements. Previously we have demonstrated FET-based intracellular recording with kinked nanowire structures[10], but the kink configuration and

device design places limits on the probe size and the potential for multiplexing. Here we report a new approach where a SiO$_2$ nanotube is synthetically integrated on top of a nanoscale FET. After penetrating the cell membrane, the SiO$_2$ nanotube brings the cell cytosol into contact with the FET and enables the recording of intracellular transmembrane potential. Simulations show that the bandwidth of this branched intracellular nanotube FET (BIT-FET) is high enough for it to record fast action potentials even when the nanotube diameter is decreased to 3 nm, a length scale which is well below that accessible with other methods[1,2,4]. Studies of cardiomyocyte cells demonstrate that when brought close, the nanotubes of phospholipid-modified BIT-FETs spontaneously penetrate the cell membrane to yield stable, full-amplitude intracellular action potential recording, showing that a stable tight seal forms between the nanotube and cell membrane. We also show that multiple BIT-FETs can record multiplexed intracellular signals from both single cells and networks of cells.

Our BIT-FET (Fig. 1a) is a combination of a Si nanowire (SiNW) FET detector and an electrically-insulating SiO$_2$ nanotube that connects the FET to the intracellular fluid (the cytosol). When there is a change in transmembrane potential, V_m, such as during an action potential, the varying potential of the cytosol inside the nanotube yields a change in the SiNW FET conductance, (G), in a manner equivalent to a time-varying potential applied to a gate electrode in a traditional FET. The polarity of the change in G will be inverted with respect to the varying V_m for a p-type FET under constant source/drain (S/D) bias as used in our studies (right panel, Fig. 1a). This BIT-FET design uses the tip of a size-controllable nanotube to interface with cells, which represents the smallest ultimate probe size (enabled by the use of the FET

sensor). Because the nanotube is built on top of the planar FET, BIT-FET arrays can fully exploit the high density of planar nanoFETs in contrast to previous work[10].

The BIT-FET devices are prepared in a sequence of growth and fabrication steps that enable control of key individual device parameters and the density of multiple devices as shown schematically in Figure S1. Ge nanowire (GeNW) branches grown on top of SiNWs from Au-nanocluster catalyzed vapor-liquid-solid mechanism[13] were used as sacrificial templates for the nanotubes (see Supplementary Methods). Representative scanning electron microscopy (SEM) images (Fig. 1b) show both an Au nanodot (inset)and the resulting GeNW branch 'standing-up' on the SiNW and oriented nearly normal to the substrate surface. After defining the S/D contacts on each side of selected GeNWs (Fig. S1d), a conformal, controlled-thickness SiO_2 layer deposited by atomic layer deposition (ALD)[14] provides the nanotube wall and S/D passivation (see Supplementary Methods). Representative SEM images of the resulting structure show clearly this conformal SiO_2 shell and the GeNW core (Figs. 1c and S2).

Finally, the BIT-FET devices fabrication is completed by two etching steps (Figs. S1f-i). The first one is to selectively remove the topmost part SiO_2 shell by buffered hydrofluoric acid (BHF) to expose the GeNW core, and the second one is to etch away the GeNW and then leave a hollow SiO_2 nanotube on SiNW. SEM images of the resulting branched SiO_2 nanotube on the SiNW structure (Fig. 1d) confirm the open end of the nanotube. Comparison of images before and after GeNW etching (Fig. 1c vs. 1d; Fig. S2 vs. insets of Fig. 1d) further shows that the nanotube structure is open to the SiNW surface as evidenced by bright to dark image contrast change associated with removal of the Ge. In addition, these images demonstrate that the SiO_2 shell is tapered at the tip: for 50 nm GeNW and 50 nm ALD SiO_2 used here, the very tip of the nanotube is about 55 nm in outer diameter and increases to a maximum of 150 nm about 2.2 μm

away from the tip. This tapering effect results from the isotropic etching of BHF (see Supplementary Methods) and we believe that it is especially attractive for decreasing the size of the probes.

We have characterized the electrical properties of the BIT-FETs and several control devices in solution to elucidate the behavior of this new device architecture. A SEM image (Fig. 2a) shows a representative two-FET structure, where a BIT-FET and conventional FET with similar channel length were fabricated with a common S electrode on the same SiNW. In both devices, the SiNW and electrodes exposed to solution are passivated with about 50 nm ALD SiO_2 as described above. Measurements of conductance (G) for both devices as a function of water-gate voltage (V_{wg}) prior to etching the GeNW core of the BIT-FET (Fig. 2b) show very little change, with sensitivity of ca. -170 nS/V. Significantly, measurements made on the same devices after removal of the GeNW core to yield an open nanotube structure (Fig. 2c), demonstrate a large increase in the sensitivity of the BIT-FET to -4530 nS/V, while the control SiNW FET shows no change. Taken together these results validate that BIT-FET devices respond selectively and with high-sensitivity to the solution inside vs. outside the nanotubes, and thus meet the requirements for intracellular recording outlined schematically in Fig. 1a. The difference in sensitivity of the BIT-FET devices to solution inside vs. outside the nanotubes originates primarily from the gate capacitance difference[11,12]. Specifically, Ge over-coating on the SiNW may lead to a larger contact area between the SiNW and the internal solution of the nanotube (the *active* FET area) than defined by the nanotube inner diameter, which can increase this sensitivity difference (see Supplementary Methods).

We have also characterized the temporal response of BIT-FET devices to assess their capability for recording fast cellular processes. A pulsed V_{wg} with 0.1 ms rise/fall time, 1 ms

duration and 100 mV amplitude was applied to approximate an action potential. The conductance exhibits a peak (dip) coincident with the 0.1 ms rise (fall) of the pulse, and a plateau step down during the constant 100 mV portion of the pulse (Fig. 2d). For pulsed V_{wg} measurement with different rise/fall times from 0.1 to 50 ms, the conductance change associated with the baseline to plateau is independent of the pulse rise time (Fig. 2e), and moreover, this change is consistent with the device sensitivity determined from quasi-static measurements (e.g., Fig. 2c).

The peak and dip features in the pulsed V_{wg} results correspond to the expected capacitive charging[15] of the passivated metal electrodes and are not intrinsic to the BIT-FET. Specifically, a control pulsed V_{wg} measurement made on a SiNW FET without a nanotube branch showed the same peak (dip) features associated with the rapid rise (fall) of the V_{wg} pulse (Fig. S4a). These capacitive features can be readily removed from the BIT-FET and control devices data to yield the pure FET response (red curves, Fig. 2d and S4a, see Supplementary Methods), and in the case of the BIT-FET, it demonstrates clearly that the conductance change follows the 0.1 ms V_{wg} pulse rise/fall without detectable delay. The results shown in Fig. 2d and e demonstrate that the BIT-FET can faithfully record potential changes with *at least* a 0.1 ms time resolution. Indeed, our modeling (below) shows the temporal resolution, which is beyond our measurement capabilities, should be much better than this value. We also note these capacitive features are not expected in cellular measurements because (i) metal electrodes are only coupled to extracellular media, where the potential changes are quite small[16] and (ii) these changes will be localized on the size of a cell, which is much smaller than the electrode area exposed to solution ($\sim cm^2$) in the pulsed V_{wg} experiments here.

In addition, we have modeled the BIT-FET device to estimate the bandwidth, which is beyond our current measurement limit, and also investigated the bandwidth dependence on

nanotube diameter. The signal transduction in the BIT-FET device can be readily solved by the classical transmission line model[15]. In our analysis (Fig. S4b, see Supplementary Methods), we determine the change of the potential at the SiNW FET surface, V_n, as a function of time following a step change of transmembrane potential at the nanotube opening to V_0. For a typical nanotube (inner diameter = 50 nm; ALD SiO_2 thickness = 50 nm; length = 1.5 μm), the calculated response (inset, Fig. 2f) yields a bandwidth of ca. 1.2 MHz. This represents an upper limit assuming the *active* FET area and relevant device capacitance C_{NW} (Fig. S4b) is defined only by the nanotube inner diameter, and could be reduced to 0.2 MHz if we assume the entire SiNW surface is *active* due to Ge over-coating (see Supplementary Methods). A summary of results (Fig. 2f) shows that the BIT-FET can achieve a bandwidth ≥ 6 kHz, which is sufficient for recording a rapid neuronal action potential[1,2], for nanotube inner diameters as small as 3 nm (fixed length = 1.5 μm). The high bandwidth determined for the BIT-FET devices results in large part from the small device capacitance, despite the increasingly large solution resistance within the nanotube with decreasing inner diameter (see Supplementary Methods). The small diameters accessible with the BIT-FET suggest that it could be minimally-invasive and capable of probing the smallest cellular structures, including neuron dendrites and dendritic spines, which are difficult using conventional electrical-based techniques[17,18].

We investigated the capability of the BIT-FET to record intracellular signals using spontaneously beating embryonic chicken cardiomyocyte cells, which were cultured on thin pieces of polydimethylsiloxane (PDMS) as described previously[16]. After modifying the devices with phospholipids[10] to facilitate the internalization of nanotubes into cells, the PDMS/cell sheet was manipulated to put a cell into gentle contact with the nanotube of a BIT-FET under standard electrophysiology microscope (see Supplementary Methods). Approximately 45s after gentle

contact was made and in the absence of applied force to the cell substrate, the recorded data showed a dramatic change (Fig. 3a). Before the transition, the signal exhibits a relatively flat baseline with small biphasic peaks (5~8 mV amplitude; ~1 ms duration) with ca. 1 Hz frequency (e.g., Figs. 3b, c). These peaks are coincident with cell beating and consistent with extracellular recording reported previously[16]. Then the baseline shifts ca. -35 mV and new peaks with 75-100 mV amplitude and ~200 ms duration are observed (Fig. 3a). The recorded conductance data yields inverted peaks for the p-type SiNW FETs used here, although the calibrated potentials are consistent with standard peak polarity and shape of intracellular action potentials. These peaks (e.g., Fig. 3d) have the shape and features characteristic of an intracellular action potential of cardiomyocyte cells[10,19,20], including fast depolarization at the beginning of the peak, plateau region, fast repolarization, and hyperpolarization and return to baseline. The signal transition from extra- to intracellular indicated the penetration of the cell by the nanotube. The baseline shift is similar with that measured recently using kinked-nanowire probes[10], but smaller than the standard resting potential for cardiomyocytes[19,20]. Our reproducible and stable recording of full-amplitude action potentials, which is a central result of our work, suggests that this baseline difference is not due to poor sealing during nanotube internalization. We propose that the discrepancy in resting potentials here could be attributed to a stronger suspension effect introduced by the intracellular polyelectrolytes at the junction[21,22] due to an order of magnitude smaller size of SiO_2 nanotube opening than a typical patch clamp pipette, although more detailed studies will be required to quantitatively understand the origin of this effect. Although the nanotube diameter routinely used in our intracellular recording studies, 50 nm inner diameter and 55 nm tip outer diameter, is larger than the smallest achievable for BIT-FETs (Fig. 2f), it is still

much smaller than the size of typical glass micropipettes[1,2] and metal microelectrodes[3,4,7] used for intracellular studies.

The change from extracellular to intracellular signal without external force applied to cell suggests the spontaneous penetration of cell membrane by the nanotube versus mechanical insertion. We speculate that lipid fusion[23,24] may play an important role in this penetration similar to our previous observations[10], and also that the small nanotube size is likely beneficial for this lipid fusion process and the formation of a tight seal. There are several attractive consequences of the spontaneous penetration. First, this typically leads to full-amplitude action potential recording (e.g., Fig. 3) without circuitry to compensate for probe-membrane leakage, thus suggesting tight sealing between the nanotube and cell membrane. Indeed, control experiments carried out without phospholipids modification of the BIT-FETs required external forces to achieve the transition to intracellular action potential signals, and the smaller amplitude of these signals, 10-30 mV, suggests leakage at the nanotube-membrane interface[3]. Second, we find that spontaneous penetration occurs in the same way for a broad range of nanotube orientation (i.e., within 30° of the surface normal), which contrasts mechanical insertion. Third, we believe that the tight nanotube-membrane seal and the very small nanotube internal volume, ca. 3 aL, help to preserve cell viability and a stable signal over time. In general, we find that termination of signal recording by the BIT-FET is due to random separation of the nanotube from the motion of the beating cardiomyocyte cell and not cell death or degradation of the nanotube/cell membrane interface, where the latter normally occur during recording with glass micropipettes[1,2]. In addition and unlike a glass micropipette, when the BIT-FET nanotube is separated from a cell (on purpose as shown below or by the beating motion), the nanotube can re-penetrate into the same cell multiple times at approximately the same position without

affecting the cell or recorded signal (see below). Last, we note that the total recording time from multiple penetrations at a given position on a cell with the BIT-FET can exceed an hour.

We also find that the BIT-FET devices are robust and reusable. Specifically, following retraction of the cell substrate from the device, which results in return of the conductance to the extracellular baseline, subsequent gentle contact of the nanotube to the same cell without changing position leads to the development of stable intracellular action potential signals again (Fig. 3e). We have repeated the gentle contact/intracellular recording/retraction cycle up to five times with the same BIT-FET nanotube near the same position on the cell without observable change in the beating frequency and action potential features. A SEM image of the BIT-FET device following these repeated cycles (Fig. S5) shows that the nanotube remains intact with some residue on the upper outer surface. In addition, we did not see evidence for the blockage of the nanotube during these cycles, which we attribute to spontaneous penetration versus suction or mechanical insertion. Furthermore, we note that devices can even be reused after being dried. Taken together these results demonstrate the reliability and robustness of the BIT-FETs and strongly indicate that this is a minimally-invasive intracellular recording technique.

A unique feature of the BIT-FET design is the straightforward fabrication of multiple, independent devices to enable multiplexed recording from single cells through cell networks. For example, we have readily aligned two phospholipid-modified BIT-FET devices separated by about 20 μm with a single, beating cardiomyocyte cell (Fig. 4a). Following gentle contact, conductance versus time measurements made simultaneously from both devices (Fig. 4b) show that device-1 first bridged the cell membrane to yield clear intracellular signals, and ~10s later we observed the development of intracellular peaks from device-2. Subsequently, intracellular signals were recorded from both devices (e.g. Fig. 4c). We can glean several important points

from these data. First, the sequential nature by which the intracellular signals develop, in the absence of an applied force, strongly supports the suggestion above that penetration of the phospholipid-modified nanotubes is a spontaneous biomimetic process that does not adversely affect the cell rather than mechanical insertion. Second, the intracellular peaks recorded simultaneously by devices-1 and -2, with full amplitude of 75-100 mV, and stable cell beating over time are consistent with the tight seal being established between the cell membrane and the nanotubes in both devices. In addition, we have also demonstrated that multiplexed measurements with BIT-FETs can be extended to cell networks (Figs. 4d & e), where we record intracellular action potentials simultaneously from different sites in a monolayer of beating cardiomyocyte cells. In the future, we note that this BIT-FET design is implementable on high density integrated planar nanoFETs, either large arrays of nanowire FETs[25] or conventional top-down nanoFET arrays[26], to enable multiplexed recording at a far higher density than demonstrated in these initial studies.

Additional work remains to improve further the BIT-FET based intracellular measurement technique. The signal-to-noise ratio is still lower than that of glass micropipette. And implementing the capability for cell stimulation in addition to recording is also important for intracellular study. However, we believe the advantages of the BIT-FET demonstrated in this work, including the capability to realize sub-5 nm size probes, the formation of tight nanotube-cell membrane seals, and the potential for large-scale high-density multiplexed recording, make it an attractive new measurement tool to extend substantially the scope of fundamental and applied electrophysiology studies to regimes hard to access by current methods.

Methods Summary

SiNWs were synthesized using Au-nanocluster catalysed VLS growth described previously[16]. After dispersing SiNWs on Si_3N_4 surface of silicon wafers, Au nanodots were defined on the top surfaces of the SiNWs by electron-beam lithography (EBL) and metal evaporation, and GeNW branches were grown from these nanodots by another Au-catalysed VLS step. Source and drain metal contacts were defined by EBL and metal evaporation on each side of selected GeNW branches on the corresponding SiNW backbones, and then a conformal and uniform SiO_2 layer was then deposited on the entire chip by ALD. Photoresist was spin-coated with thickness smaller than the selected GeNW branches height, and then BHF was used to remove the SiO_2 from the exposed tips of the GeNW/SiO_2 core/shell structure. Following photoresist lift-off, H_2O_2 was used to etch the GeNW cores and yield the final BIT-FET devices. Conductance versus V_{wg} measurements were carried out in 1×PBS buffer using an Ag/AgCl electrode. Electrical recordings from embryonic chicken cardiomyocytes were carried out using methods published previously[10,16], with cells cultured on thin PDMS films and device chips modified with lipid layers. A glass micropipette was used to control the relative position between the cell and the nanotube(s) of BIT-FET device(s), and Ag/AgCl reference electrodes were used to fix the extracellular solution potential. The BIT-FET bandwidth as a function of nanotube ID was determined from simulations of the time-dependent change in potential at the SiNW FET surface, V_n, following a potential step change at the open nanotube end.

References:

1. Sakmann, B. & Neher, E. Patch clamp techniques for studying ionic channels in excitable membranes. *Ann. Rev. Physiol.* **46**, 455-472 (1984).

2. Molleman, A. *Patch clamping: an introductory guide to patch clamp electrophysiology* (Wiley, Chichester, England, 2003).

3. Rutten, W. L. C. Selective electrical interfaces with the nervous system. *Annu. Rev. Biomed. Eng.* **4**, 407-452 (2002).

4. Purves, R. D. *Microelectrode methods for intracellular recording and ionophoresis* (Academic Press, London, 1981).

5. Chorev, E., Epsztein, J., Houweling, A. R., Lee, A. K. & Brecht, M. Electrophysiological recordings from behaving animals-going beyond spikes. *Curr. Opin. Neurobiol .* **19**, 513-519 (2009).

6. Dunlop, J., Bowlby, M., Peri, R., Vasilyev, D. & Arias, R. High-throughput electrophysiology: an emerging paradigm for ion-channel screening and physiology. *Nat. Rev. Drug Discovery* **7**, 358-368 (2008).

7. Hai, A., Shappir, J. & Spira, M. E. In-cell recordings by extracellular microelectrodes. *Nat Methods.* **7**, 200-U50 (2010)

8. Schrlau, M. G., Dun, N. J., & Bau, H. H. Cell electrophysiology with carbon nanopipettes. *ACS Nano* **3**, 563-568 (2009).

9. de Asis, E. D., Leung, J., Wood, S., & Nguyen, C. V. High spatial resolution single multiwalled carbon nanotube electrode for stimulation, recording, and whole cell voltage clamping of electrically active cells. *Appl. Phys. Lett.* **95**, 153701 (2009).

10. Tian, B. *et al*. Three-dimensional, flexible nanoscale field-effect transistors as localized bioprobes. *Science* **329**, 831-834 (2010).

11. Sze, S. M. & Ng, K. K. *Physics of Semiconductor Devices, 3rd Edition* (Wiley-interscience, 2006).

12. Patolsky, F., Zheng, G. & Lieber, C. M. Nanowire-Based Biosensors. *Anal. Chem.* **78**, 4260-4269 (2006).

13. Jiang, X. *et al.*, Rational growth of branched nanowire heterostructures with synthetically-encoded properties and function. *Proc. Natl. Acad. Sci. USA* **108**, 12212-12216 (2011).

14. Hausmann, D., Becker, J., Wang, S. & Gordon, R. G. Rapid vapor deposition of highly conformal silica nanolaminates. *Science* **298**, 402-406 (2002).

15. Sadiku, M. N. O. *Elements of Electromagnetics. 3rd edition*. (Oxford University Press, USA, 2000).

16. Cohen-Karni, T., Timko, B. P., Weiss, L. E. & Lieber, C. M. Flexible electrical recording from cells using nanowire transistor arrays. *Proc. Natl. Acad. Sci. USA* **106**, 7309-7313 (2009).

17. Scanziani, M. & Hausser, M. Electrophysiology in the age of light. *Nature* **461**, 930-939 (2009).

18. Davie, J. T. *et al*. Dendritic patch-clamp recording. *Nat. Protoc.* **1**, 1235-1247 (2006).

19. Bers, D. M. Cardiac excitation-contraction coupling. *Nature* **415**, 198-205 (2002).

20. Zipes, D. P. & Jalife, J. Cardiac electrophysiology: from cell to bedside, 5th edition (Saunders, Philadelphia, PA, 2009).

21. Buck, R. P. & Grabbe, E. S. Electrostatic and thermodynamic analysis of suspension effect potentiometry. *ANAL. CHEM.* **58**, 1938-1941 (1986).

22. Tasaki, I. & Singer, I. Some problems involved in electric measurements of biological systems. *ANN. NY. ACAD. SCI.* **148**, 36-53 (1968).

23. Chernomordik, L. V. & Kozlov, M. M. Mechanics of membrane fusion. *Nature Struct. Mol.Biol.* **15**, 675-683 (2008).

24. Almquist, B. D. & Melosh, N. A. Fusion of Biomimetic Stealth Probes into Lipid Bilayer Cores. *Proc. Natl. Acad. Sci. USA* **107**, 5815-5820 (2010).

25. Yan, H. *et al*. Programmable nanowire circuits for nanoprocessors. *Nature* **470**, 240-244 (2011).

26. International Technology Roadmap for Semiconductors. Available online at http://www.itrs.net. (2009 Edition).

Author Contributions X.D. and C.M.L. designed the experiments. X.D., R.G, T.C.-K., Q.Q., H.S.C. and B.T. performed experiments. X.D., P.X. and Q.Q. performed modeling and analyses. X.D., P.X., Q.Q. X.J. and C.M.L.

analyzed data. X.D., P.X., and C.M.L. wrote the paper. All authors discussed the results and commented on the manuscript.

Competing financial interests: The authors declare that they have no competing financial interests.

Figure Legends

Figure 1. **Schematics and structural characterization of the BIT-FET. a**, schematics showing (left) a cell coupled to a BIT-FET and (right) the variation in device conductance, (*G)*, during an action potential, where S, D, V_m, and *t* correspond to source electrode, drain electrode, membrane potential, and time, respectively. The SiO_2 nanotube connects the cytosol (orange) to the p-type SiNW FET, and together with the SiO_2 passivation excludes the extracellular medium (light blue) from the *active* device channel. The schematic structures on the membrane represent different ion channels, and are not scaled to the true size of the BIT-FET. **b**, SEM image of a GeNW branch on a SiNW with an orientation near the surface normal. Inset, SEM image of an Au nanodot on a SiNW prior to GeNW growth. **c**, SEM image of a GeNW/SiNW heterostructure coated with ALD SiO_2. Magnified images of the top and bottom are shown in Fig. S2. **d**, SEM image of a final nanotube on a SiNW. Insets, magnified images of the top and bottom of the nanotube. Scale bars, 100 nm in inset of **b**, 200 nm in all others.

Figure 2. Water gate characterization and bandwidth analysis. a, SEM image of a BIT-FET device (S-D_1) and control device (S-D_2). **b** and **c**, Water gate, V_{wg}, responses prior to and after GeNW etching, respectively. Blue, (S-D_1); red, (S-D_2). **d**, pulsed V_{wg} with 0.1 ms rise/fall time, 1 ms duration and 100 mV amplitude (upper), and the corresponding conductance change of a BIT-FET device (black, lower). The red trace is the pure field-effect response after removing the capacitive signals of the passivated metal electrodes (*see Supplementary Methods*). **e**, baseline to plateau conductance change of the same BIT-FET device as in **d** versus pulse rise/fall time. The change was measured as an average over data 0.2-0.5 ms after the start of the pulse. Pulse

amplitude was kept at 100 mV, and duration was ten times the rise/fall time in all measurements. **f**, Calculated bandwidth of the BIT-FET device versus nanotube inner diameter (ALD SiO_2 thickness was the same as the nanotube inner diameter, and the nanotube length was fixed at 1.5 μm). The black and red symbols correspond to upper and lower limits, respectively (*see Supplementary Methods*). Inset, calculated change of the potential at the SiNW FET surface V_n (normalized with the step change V_0 of potential at the nanotube opening) versus time.

Figure 3. Intracellular action potential recording. a, a representative trace reflects the transition from extra- to intra- cellular recording. **b**, magnified trace of the part in the black dashed rectangle in **a**. **c**, magnified trace of the peak in the blue dashed rectangle in **b**. The stars in **b** and **c** mark the position of extracellular spikes. **d**, magnified trace of the peak in red dashed rectangle in **a**. **e**, the trace corresponding to the second entry of the nanotube around the same position on the cell. The potential was calibrated using the sensitivity values measured on phospholipid-modified devices by quasi-static V_{wg} measurement (e.g. blue trace in Fig. 2**c**) and pulsed V_{wg} measurement with 0.1 ms pulse rise/fall time (same for Fig. 4). The sensitivity obtained from these two measurements is same as discussed before.

Figure 4. Multiplexed intracellular recording. a, Differential interference contrast microscopy (DIC) image of two BIT-FET devices (position marked with dots) coupled to a single cardiomyocyte cell, with cell boundary marked by the yellow dashed line. **b**, The simultaneously recorded traces from the two devices in **a**, corresponding to the transition from extra- to intra- cellular signal. The transition happened in sequential manner. The break mark labels the ~1 s discontinuity between the two adjacent traces.

c, representative trace of stable intracellular action potentials recorded ~120 s after the internalization of the devices in **a**. **d**, DIC image of three BIT-FET devices coupled to a layer of beating cardiomycyte cell network (from a different PDMS/cell sample than in **a**). **e**, representative traces recorded simultaneously from the devices shown in **d**. The three devices exhibit intracellular action potential signals from different cells in the cell network. We note that devices used in **a** and **d** have different sensitivities (and are also different from the one used in Fig. 3). These differences are primarily due to variations in Ge over-coating during GeNW growth (see Supplementary Information). The potential was calibrated using the sensitivity values measured for each individual device, and all devices yield corresponding intracellular action potential values with full amplitude of 75-100 mV (independent of this conductance/sensitivity variation).
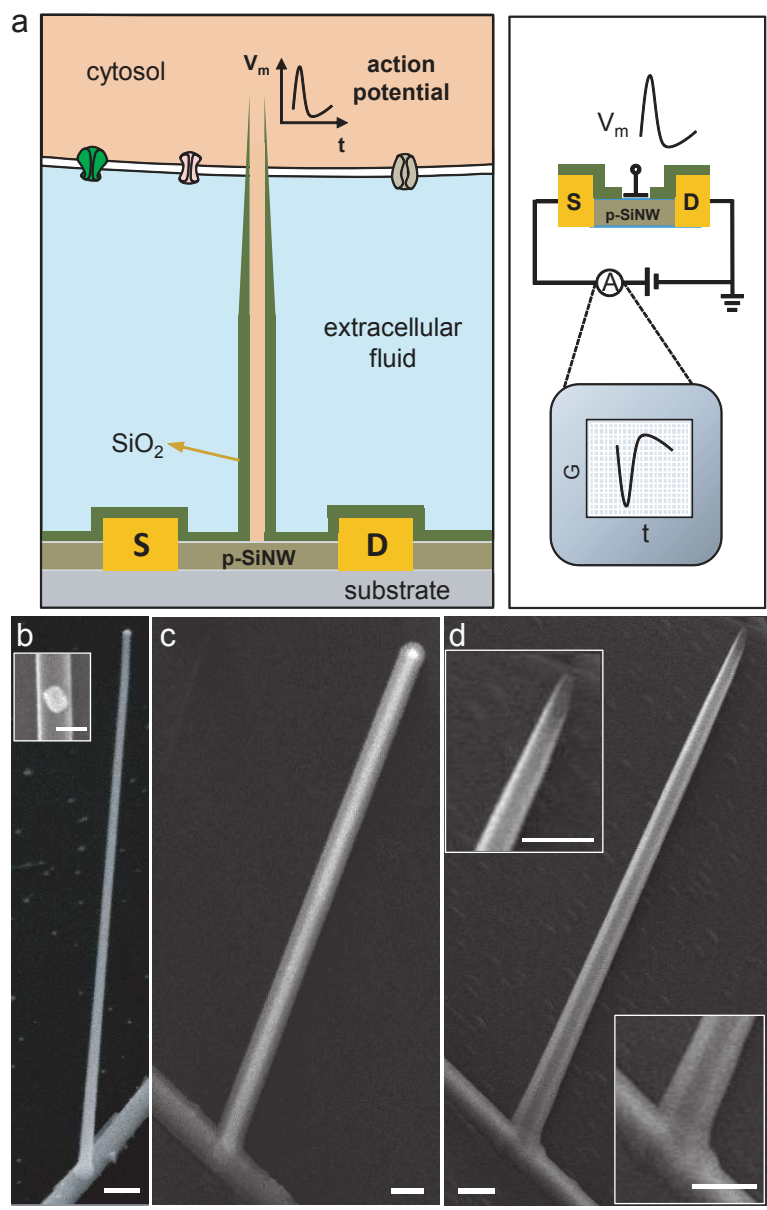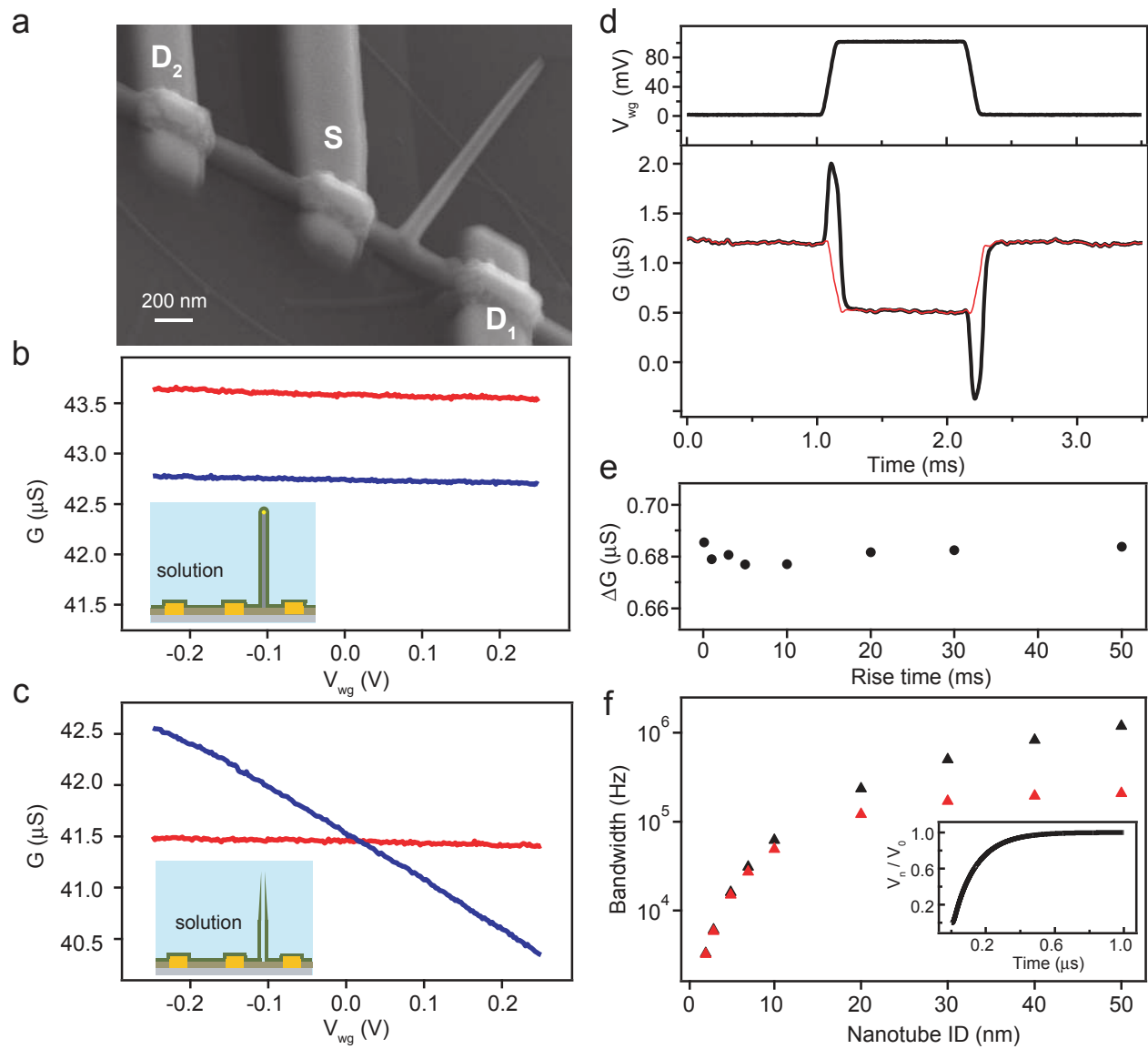
a

cytosol

V_m

action potential

t

extracellular fluid

SiO_2

S   p-SiNW   D   substrate

V_m

S   p-SiNW   D

A

G   t

b

c

d

Figure 1

a

D₂

S

D₁

200 nm

b

G (µS)

43.5

43.0

42.5

42.0

41.5

solution

-0.2   -0.1   0.0   0.1   0.2

V_wg (V)

c

G (µS)

42.5

42.0

41.5

41.0

40.5

solution

-0.2   -0.1   0.0   0.1   0.2

V_wg (V)

d

V_wg (mV)

80

40

0

G (µS)

2.0

1.5

1.0

0.5

0.0

0.0   1.0   2.0   3.0

Time (ms)

e

ΔG (µS)

0.70

0.68

0.66

0   10   20   30   40   50

Rise time (ms)

f

Bandwidth (Hz)

10⁶

10⁵

10⁴

V_n/V_0

1.0

0.6

0.2

0.2   0.6   1.0

Time (µs)

0   10   20   30   40   50

Nanotube ID (nm)

Figure 2

a 1st entry

20 mV | 200 nS
1 s

b ★ ★ ★

3 mV | 30 nS
500 ms

c 3 mV | 30 nS
10 ms
★

d 20 mV | 200 nS
100 ms

e 2nd entry

20 mV | 200 nS
1 s

Figure 3

a

Device-1
Device-2

10 μm

b

67.06
67.04
67.02

G (μS)

Device-1

34.86
34.83
34.80

Device-2

2 s

c

67.04
67.02
67.00

G (μS)

Device-1

34.86
34.83
34.80

Device-2

2 s

d

Device-3
Device-2
Device-1

30 μm

e

2.88
2.73

G (μS)
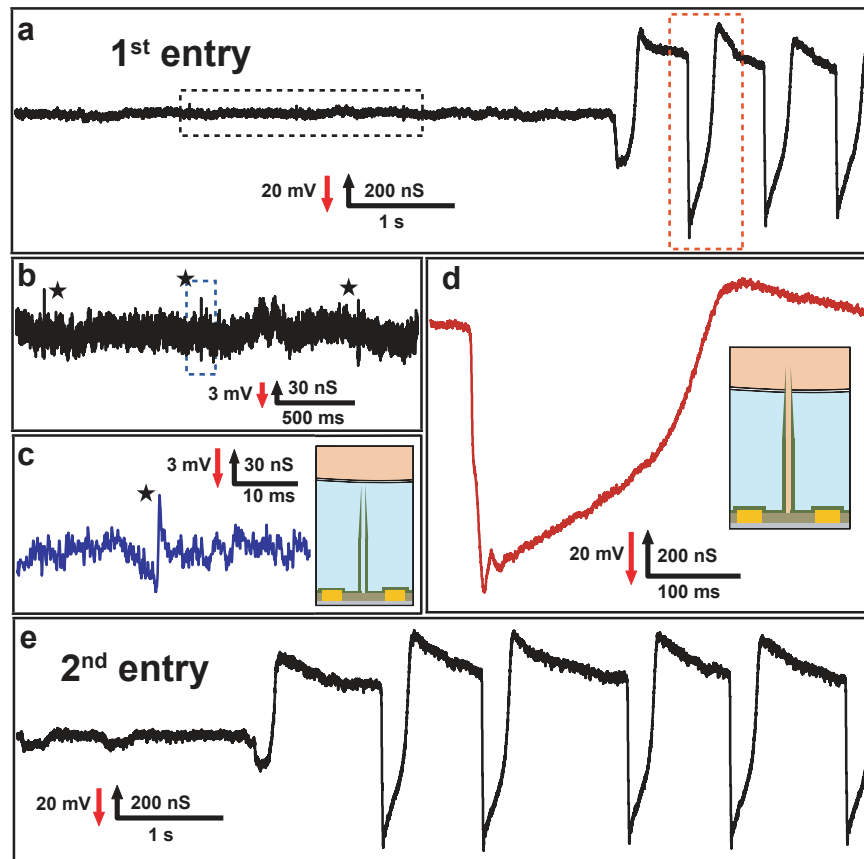
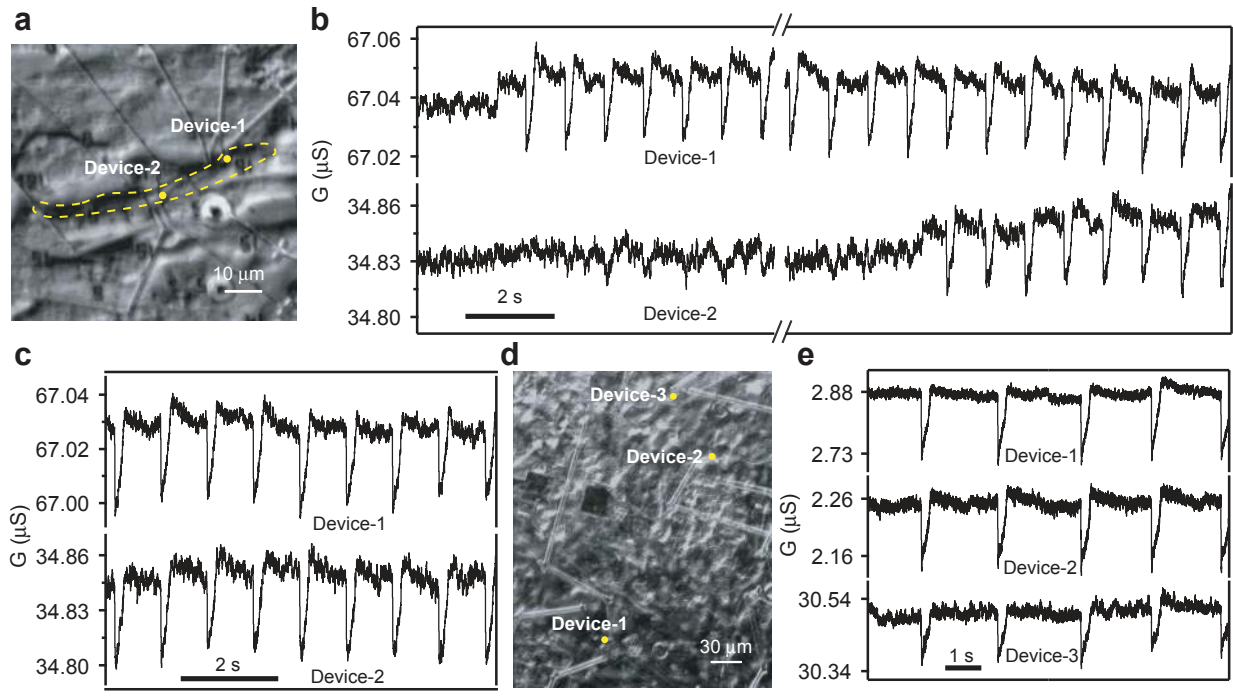Device-1

2.26
2.16

Device-2

30.54
30.34

Device-3

1 s

Figure 4

Supplementary Information for:

Intracellular recordings of action potentials by an extracellular nanoscale field-effect transistor

Xiaojie Duan, Ruixuan Gao, Ping Xie, Tzahi Cohen-Karni, Quan Qing, Hwan Sung Choe, Bozhi Tian, Xiaocheng Jiang, and Charles M. Lieber

This PDF file includes:
Materials and Methods
Supplementary Figures S1-S5
Supplementary references

Materials and Methods

Nanowire nanostructure synthesis. Single crystal p-doped silicon nanowires (p-SiNWs) were synthesized by the nanocluster-catalyzed vapor-liquid-solid (VLS) process as described previously[1]. Briefly, 100 nm diameter gold nanoparticles (Ted Pella) were dispersed on SiO_2/Si growth substrates (Nova Electronic Materials), and growth was carried out at a total pressure of 25 torr, temperature of 450–460 °C, using SiH_4 (2.5 sccm), B_2H_6 (3 sccm, 100 ppm in He) and Ar carrier (10 sccm) for 20~30 mins. The resulting ca. 100 nm diameter p-SiNWs grown as above were deposited from an isopropanol dispersion onto Si_3N_4 surface of silicon wafers (100 nm thermal SiO_2, 200 nm Si_3N_4, n-type, 0.005 V · cm, Nova Electronic Materials). Germanium nanowire (GeNW) branches, which serve as the template for the final nanotube structures, were also synthesized by the Au nanocluster catalyzed VLS process. A modification of the sequential branch growth process described previously[2] was used (Figs. S1a-c). First, Au nanodots were defined by electron-beam lithography (EBL, JEOL JSM-7000F) and metal evaporation on the top surfaces of the dispersed SiNWs, the chip was placed in the growth reactor, and then GeNW branches were grown using an initial nucleation step at 305-315 °C for 5 min (GeH_4 (10 sccm, 10% in H_2), H_2 (200 sccm), total pressure of 100 torr) and elongation step at 280-295 °C for 20 min (gas flow and pressure same as for nucleation). The GeNW branch diameter, which defines the final SiO_2 nanotube inner diameter (ID), is controlled through the size and thickness of the deposited Au nanodots. And the growth with Au nanodots of 80 nm diameter and 40 nm thickness yielded average 50 nm GeNW branches on top of SiNW backbones. The GeNW lengths are determined by the growth time with typical values of 2-4 μm. The specific orientation of the GeNWs was not controlled in these studies because the penetration of the nanotubes into cells does not require them to be vertical (see main text). For this reason, we selected and used GeNWs within 30° with respect to the surface normal for BIT-FET devices (see below). We note that alternative methods, such as chemical reduction from solution, can be used to prepare Au particles on SiNWs (without the need for EBL) for GeNW branch growth[2] in a parallel and high-throughput manner.

BIT-FET device fabrication. Completion of the nanotube structure and device fabrication were carried out in parallel as shown schematically in Fig. S1. Following GeNW branch growth, resist was coated on the chip (~2 μm copolymer, MMA (8.5) MAA (EL11) and ~0.5 μm PMMA (950

C5), MicroChem Corp.), baked at 180 °C for 10 min. Then EBL and thermal evaporation were used to define Ti/Pd/Ti (1.5/120/10 nm) S/D contacts on each side of selected GeNW branches, which are within 30° with respect to the surface normal, on the corresponding SiNW backbones (Fig. S1d). The typical separation between S/D contacts was 300-700 nm. Critical point drying (Auto Samdri 815 Series A, Tousimis,) was used during lift-off and rinse steps to minimize collapse of the GeNW branches. A uniform layer of SiO_2 (~50 nm) was deposited by atomic layer deposition (ALD, Savannah-S200, Cambridge NanoTech) at 250 °C[3], and annealed in the ALD system at 250 °C for 15 min. The conformal SiO_2 layer (Fig. S1e) serves both as the nanotube wall (after removal of Ge) and passivation of the metal electrodes. The GeNW core is removed by a sequence of steps shown in Fig. S1 (f-i) to yield the final nanotube device. First, A photoresist protection layer (Shipley S1813 or S1818, MicroChem Corp.) was coated to a thickness smaller than the GeNWs height, baked at 115 °C for 5 min, and then the exposed SiO_2 of the GeNW/SiO_2 core/shell structure was removed by BHF (Buffered HF Improved, Transene) (20~25 s for ~50 nm ALD SiO_2). The BHF etching goes along both the radial and axial direction, which results in a tapered SiO_2 shell. Following photoresist lift-off, hydrogen peroxide (H_2O_2, 30%, Sigma) was used to selectively etch the Ge (50 ºC, 45-60 min). The final SiO_2 nanotube height is defined by the thickness of the photoresist protection layer. Unless specifically mentioned, all devices used in this work, including those for device characterization and cell measurements etc., use nanotube inner diameter and ALD SiO_2 thickness of ca. 50 nm, nanotube length of 1-1.5 μm, p-doped SiNWs with diameter of ca. 100 nm.

Device characterization. To characterize the response of the BIT–FET devices in aqueous solution, a 2 mm thick polydimethylsiloxane (PDMS) sheet with a 15 mm × 10 mm window was put on the device chip, and the open region was filled with 1× phosphate buffered saline (PBS, Mediatech, Inc.); a Ag/AgCl electrode was inserted into the solution and the FET conductance versus water gate voltage (V_{wg}) measurements were carried out by sweeping the voltage while simultaneously recording the FET current with a current preamplifier (1211, DL Instruments). The voltage sweep output/preamplifier output was generated/recorded with a DAC card (PCI-6030E, National Instruments, Inc.) under computer control, with typical ramp speed of 50 mV/s. To assess the temporal response of the BIT-FET devices, a pulsed V_{wg} with variable rise time (0.1-50 ms) was generated (Axon Digidata 1440A Data Acquisition System, Molecular Devices,

Inc.) and the current of the FET was amplified with a home-built current preamplifier, filtered (CyberAmp 380, Molecular Devices, Inc.), and then digitized (Axon Digidata 1440A Data Acquisition System, Molecular Devices, Inc.). Conductance values recorded for BIT-FET devices vary between ca. 1-70 μS. This variation reflects differences in the SiNWs and device configuration, but has no effect on calculated potentials since the sensitivity of each device was determined prior to cell measurements.

BIT-FET sensitivity. The sensitivity, which is characterized by the conductance change per unit V_{wg} change (transconductance) is proportional to the gate capacitance[4]. Before GeNW etching (Fig. S3a), the relevant gate capacitance, which reflects the sensitivity of BIT-FET to the solution outside the nanotube, can be estimated[5] with the half cylindrical model (inset, Fig. S3a) as:

$$C_{out} = \pi\varepsilon_0\varepsilon_r L / ln[(d_{SiNW} + 2t_{SiO2})/d_{SiNW}] \tag{1}$$

where $\varepsilon_0, \varepsilon_r, L, d_{SiNW}$ and t_{SiO2} are vacuum dielectric constant, relative dielectric constant of SiO_2, effective channel length, SiNW diameter and ALD SiO_2 thickness,

$$L = L_{app} - d_{base} - 4t_{SiO2} \tag{2}$$

L_{app} is the distance between the two closest edges of S/D electrodes (apparent channel length), d_{base} is the diameter of the GeNW branch base, which is normally larger than the diameter of the GeNW branch body (c.a. 100 nm for 50 nm average diameter GeNW, e.g. Fig. 1b).

After removing the GeNW, solution fills in nanotube and gates the SiNW FET through the thin (1.5 nm, t_{native} as below) native oxide (Fig. S3b). We model the capacitance, C_{in}, which reflects the sensitivity of the BIT-FET to solution inside the nanotube, as a parallel plate capacitor[5]:

$$C_{in} = \varepsilon_0\varepsilon_r A / t_{native} \tag{3}$$

where A is the contact area between the SiNW and the solution inside the nanotube. If there is no Ge over-coating, A is equal to the GeNW base area. The transconductance ratio after to before GeNW etching is estimated by the gate capacitance ratio, $(C_{in}+C_{out})/C_{out}$. For the device used in Fig. 2 a-c, this yields a ratio, ~5, which is smaller than the experimental value, ~26.

The enhanced sensitivity difference compared to the idealized calculation is a result of several factors. First, the contact area A can be larger than that defined by the GeNW branch base due to over-coating of Ge on SiNW surface during GeNW growth. Removal of this Ge material over-coated on SiNWs during etching will lead to a longer *active* channel, and larger A and C_{in}. We note that SEM images of the BIT-FETs taken after breaking nanotubes at the SiNW-tube junction always show a larger hole than would be defined by GeNW branch base alone, which is consistent with a larger A. The upper limit in this context, which corresponds to the entire SiNW surface exposed to the internal solution of the nanotube, would yield a sensitivity ratio of ~50. The experimental ratio falls between these calculated limits, which suggests that the *active* channel exposed to the internal solution of nanotube is smaller than the entire SiNW surface but larger than that defined by the GeNW base. Indeed, device measurements show a range of enhancement ratios and the transconductance/sensitivity values for different BIT-FETs vary for different GeNW growth conditions (different Ge over-coating). We note that because all device sensitivities are characterized, the observed variation does not affect our determination of absolute potential change in the cell measurements. In the future, we anticipate that Ge over-coating could be used to rationally enhance the sensitivity of the BIT-FET devices. Second, the small effective channel length L and relatively thick SiO_2 dielectric layer can lead to a reduction in C_{out} due to the screening by the metal S/D electrodes[6]. This would lead to a lower sensitivity than estimated for the BIT-FET prior to GeNW etching.

Pulsed water gate curve fitting. In the pulsed V_{wg} measurement, the capacitive coupling current between the passivated metal electrodes (in the open window area) and the solution yield +/- peaks in during the rising/falling edges of the pulse (e.g., Figs. 2d and S4a). To accurately remove these artifacts without affecting the intrinsic BIT-FET signal we carried out the following steps. First, a control device without SiO_2 nanotube was fabricated and measured (black trace, Fig. S4a), where the baseline conductance (before and after pulse) and the steady state conductance during the pulse represents the intrinsic SiNW FET response (red trace, Fig. S4a). The +/- peaks obtained by subtracting the intrinsic FET response from the measured data for the control device, yields the pure capacitive coupling signal for the control device. The capacitive coupling signal determined from this analysis for the control device was then scaled by ratio of the exposed electrode areas for the BIT-FET versus control devices, to yield the

capacitive coupling signal of the BIT-FET device, which is then subtracted from the measured data to yield intrinsic device response (red trace, lower panel of Fig. 2d). Note that the subtraction has no fitting parameters and the capacitive coupling artifacts are removed completely.

Cell recording. Embryonic chicken cardiomyocytes were cultured using published protocols on thin PDMS films[7,8]. Device chips were incubated with lipid vesicles of 1,2-dimyristoyl-sn-glycero-3-phosphocholine (DMPC, Avanti Polar Lipids Inc.) containing 1% 1-myristoyl-2-{12-[(7-nitro-2-1,3-benzoxadiazol-4-yl) amino] dodecanoyl}-sn-glycero-3-phosphocholine (NBD-lipid, Avanti Polar Lipids Inc.) as fluorescent reporter to form supported lipid layers on devices including nanotube surfaces, using a procedure described earlier[8]. The cell recording measurements were carried out in tyrode solution (pH ~ 7.3) at 30-37°C using a 100 mV DC source voltage for FET devices. The current was amplified with a home-built multi-channel current preamplifier, filtered with a 6 kHz low pass filter (CyberAmp 380), and digitized at 50-250 kHz sampling rate (Axon Digi1440A). Ag/AgCl reference electrodes were used to fix the extracellular solution potential in all recording experiments[7,8]. The PDMS/cell sheets were manipulated using glass micropipettes to control the relative position between the cells and the nanotubes.

Bandwidth calculation. The BIT-FET device was modeled by the equivalent circuit shown in Fig. S4b. Resistors R_1, …, R_{i+j} are used to model the distributed resistance of the solution inside the nanotube, capacitors C_1, …, C_{i+j} model the distributed capacitance between the inside and outside of the nanotube, R_{access} is the access resistance from the solution to the opening of the nanotube, V_0 is the intracellular potential of the cell. Outside the cell, the solution outside the nanotube is fixed by the reference electrode, V_n is the potential at the end of the nanotube (SiNW surface), C_{NW} is the gate capacitance of SiNW accessed by the internal solution in nanotube, and R_{NW} is the resistance of the SiNW. The cell electrical potential signal propagates from the opening of the nanotube to its end, where it couples to the FET channel, through the solution. The potential also capacitively couples to the solution outside the nanotube across the SiO_2 nanotube wall. Using the Ohm's law and capacitive coupling[5] at any point along the nanotube, the propagation of the electrical potential signal can be described by:

6

$$
\begin{cases}
-\dfrac{\partial V_{in}}{\partial z} = \rho_R I \\[2mm]
-\dfrac{\partial I}{\partial z} = \rho_C \dfrac{\partial (V_{in} - V_{out})}{\partial t}
\end{cases}
\tag{4}
$$

Here V_{in}, V_{out}, ρ_R, ρ_C, I, z, t are potential inside the nanotube, potential outside the nanotube, linear resistivity of solution inside the nanotube (resistance per unit length), capacitance of the nanotube wall per unit length, current, distance from the nanotube opening, and time, respectively. These equations can be rewritten as:

$$
\dfrac{\partial^2 V_{in}}{\partial z^2} = \rho_R \rho_C \left(\dfrac{\partial V_{in}}{\partial t} - \dfrac{\partial V_{out}}{\partial t} \right)
\tag{5}
$$

where ρ_R is calculated from the solution bulk resistivity ρ_{Bulk} by $\rho_R = 4\rho_{Bulk}/\pi d^2$ and ρ_C comes from three parts connected in series: the two electrical double layers on the inner and outer SiO_2 surface of the nanotube, and the capacitance across the SiO_2 wall. Each part is calculated from the cylindrical capacitor model[5] by $\rho_C = 2\pi \varepsilon \varepsilon_0 / ln(a_2/a_1)$, where ε is the dielectric constant of the material, a_1 and a_2 is the inner and outer diameter of the cylinder. For example, the capacitance across the SiO_2 wall can be written as $\rho_C = 2\pi \varepsilon_r \varepsilon_0 / ln\,[(d + 2t_{SiO2})/d]$. Here d is the nanotube inner diameter. ε_r, ε_0, and t_{SiO2} are defined as before in the 'BIT-FET sensitivity' part. Overall, the capacitance of the SiO_2 wall is the dominant term due tothe large thickness of the SiO_2 wall and the relatively small dielectric constant of SiO_2 (compared to the water double layer dielectric constant), although we considered all three parts in the calculation.

We evaluate the potential change at the end of the nanotube as a function of time following cell potential change, based on equation (5), using 1-dimensional finite element method (written in Mathematica, Wolfram Research, Inc.). The boundary conditions for the simulation are as follows: Outside the cell, V_{out} is fixed by the reference electrode; inside the cell, V_{out} equals to the intracellular potential of the cell; 1/3 of the nanotube is inside the cell; the gate capacitance, C_{NW}, of the SiNW is approximated as a parallel plate capacitor.

The bandwidth is evaluated by using a fast ramp of the cell potential from 0 to the steady-state value V_0, and simulating the corresponding change of the potential at the end of the nanotube V_n vs. time. The effective bandwidth, BW, is:

$$BW \approx 0.35 / \tau \qquad\qquad (6)$$

where τ is the time for V_n to change from 10 % to 90 % of V_0. For the calculation of the diameter-dependent bandwidth (Fig. 2f), the SiO_2 thickness was fixed at the nanotube ID, and the nanotube length was a constant 1.5 μm. The high bandwidth determined for the BIT-FET devices results in large part from the small device capacitances, despite the increasingly large solution resistance within the nanotube with decreasing ID. For example, the resistance of physiological solution inside a 10 nm ID, 1.5 μm long nanotube is ca. 19 GΩ, but the corresponding capacitance is only 0.3 fF.

The above simulation gives the upper limit bandwidth for our BIT-FETs. When the *active* channel extends beyond the area defined by the GeNW base due to the Ge over-coating (see sensitivity discussion above), the bandwidth will decrease. The lower-limit bandwidth for this configuration (red data points, Fig 2f) was calculated using the same finite element method by assuming a 10 nm gap between SiNW and ALD SiO_2, and 400 nm *active* SiNW channel length.
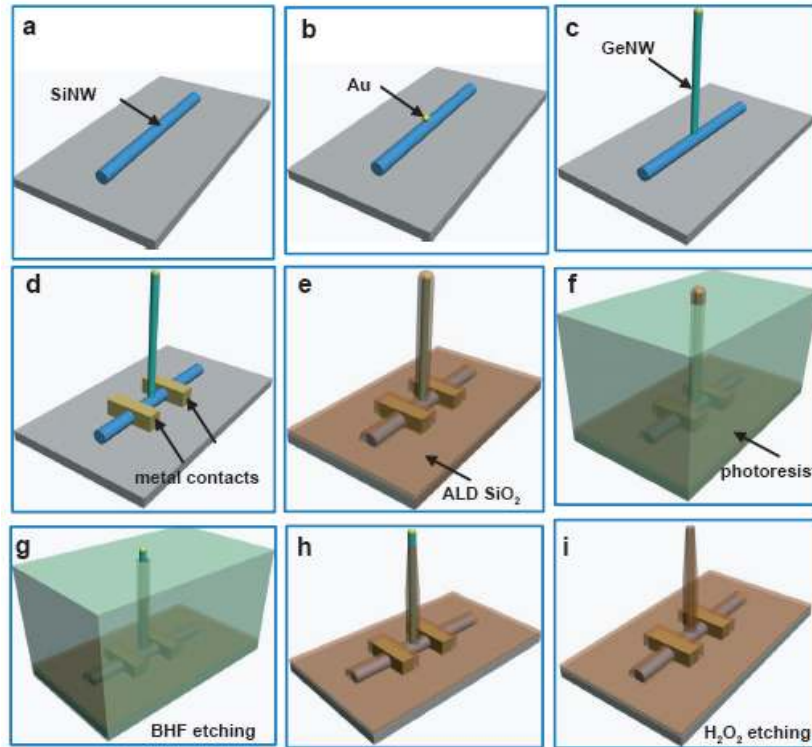
Figure S1 | Schematic fabrication flow for the BIT-FET device. a, SiNW is dispersed on substrate. **b**, Au nanodot is defined on the SiNW using EBL and thermal evaporation. **c**, GeNW is grown on top of the SiNW through Au nanodot catalyzed VLS process. **d**, EBL is used to define metal contacts on the SiNW at each side of the GeNW branch. **e**, SiO_2 is deposited by ALD to yield a conformal coating over the entire device. **f**, photoresist with thickness smaller than the GeNW branch height is coated on the chip. **g**, BHF is used to etch the SiO_2 at the tip of the GeNW branch. **h**, isotropic BHF etching of SiO_2 yields tapered nanotube with smaller SiO_2 thickness and outer diameter at the upper part of the nanotube. **i**, the GeNW is removed to yield a nanotube connected to the SiNW FET.
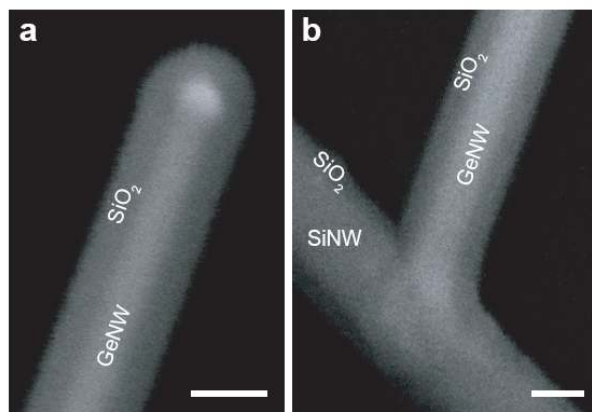
Figure S2 | High-resolution SEM images of the GeNW/SiNW structure after SiO$_2$ coating. a, b, top and bottom, respectively, of a GeNW/SiNW structure coated with ca. 50 nm SiO$_2$. scale bars, 100 nm.
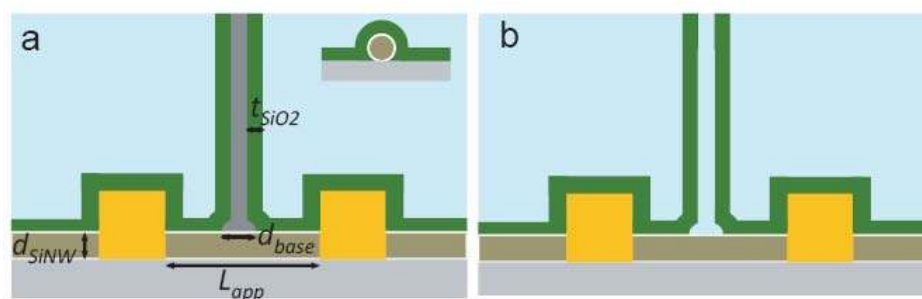
Figure S3 | Solution access to BIT-FET. a, b, schematics of the BIT-FET before and after removing the GeNW, respectively. Inset of **a**, the cross-section view of a SiNW coated with conformal ALD SiO_2, showing the half cylindrical configuration.
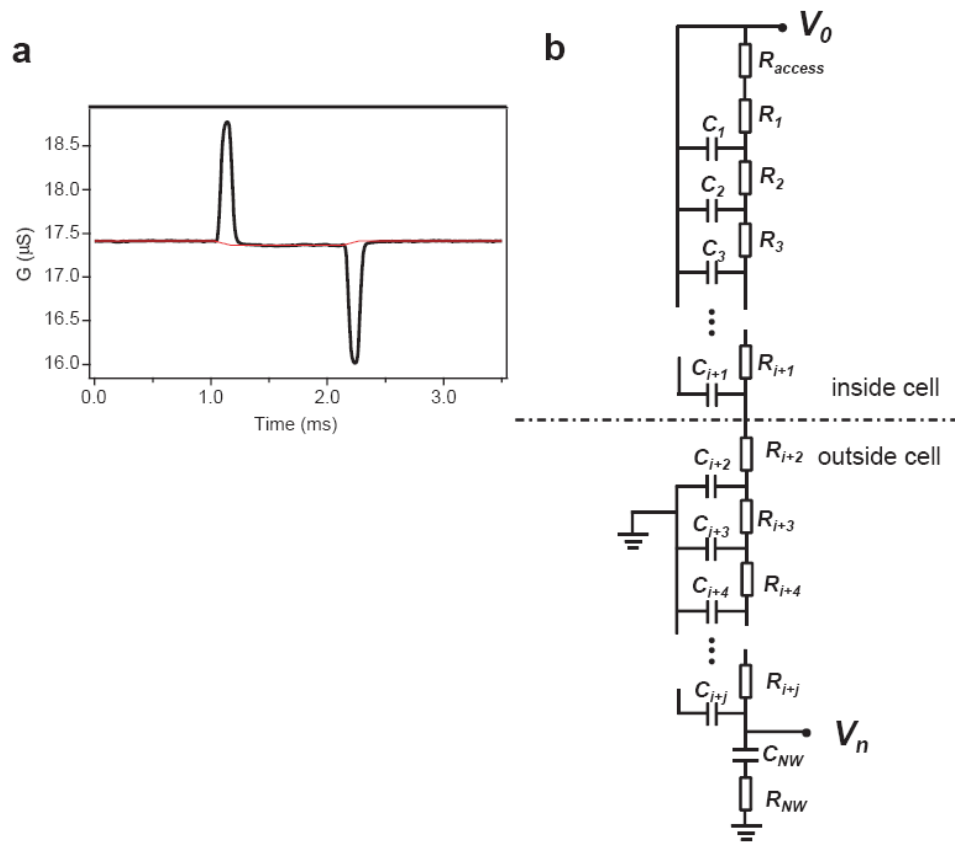
Figure S4 | BIT-FET device modelling and bandwidth analysis. a, conductance change versus time for a SiNW FET control device without nanotube (black trace) and the reconstructed intrinsic field-effect response of it (red trace). The V_{wg} pulse used had an amplitude, rise/fall time and duration of 100 mV, 0.1 ms, and 1 ms, respectively. **b**, equivalent circuit for intracellular recording by a BIT-FET device.

Figure S5 | Robustness of the BIT-FET device. SEM image of a BIT-FET device after five internalization/retraction cycles with intracellular recording achieved during each cycle. Some residue was observed on the top region of the nanotube at the completion of the multiple internalization/retraction experiment.

References

1. Patolsky, F., Zheng, G. & Lieber, C. M. Fabrication of silicon nanowire devices for ultrasensitive, label-free, real-time detection of biological and chemical species. *Nature Prot.* **4**, 1711-1724 (2006).

2. Jiang, X. *et al.* Rational growth of branched nanowire heterostructures with synthetically-encoded properties and function. *Proc. Natl. Acad. Sci. USA* **108**, 12212-12216 (2011).

3. Hausmann, D., Becker, J., Wang, S., & Gordon, R. G. Rapid vapor deposition of highly conformal silica nanolaminates. *Science* **298**, 402-406 (2002).

4. Sze, S. M., & Ng, K. K. *Physics of Semiconductor Devices, 3rd Edition* (Wiley-interscience, 2006).

5. Sadiku, M. N. O. *Elements of Electromagnetics. 3rd edition.* (Oxford University Press, USA, 2000).

6. Hu, Y., Xiang, J. Liang, G., Yan, H., & Lieber, C. M. Sub-100 Nanometer Channel Length Ge/Si Nanowire Transistors with Potential for 2 THz Switching Speed. *Nano Lett.* **8**, 925-930 (2008).

7. Cohen-Karni, T., Timko, B. P., Weiss, L. E. & Lieber, C. M. Flexible electrical recording from cells using nanowire transistor arrays. *Proc. Natl. Acad. Sci. USA* **106**, 7309-7313 (2009).

8. Tian, B. *et al*. Three-dimensional, flexible nanoscale field-effect transistors as localized bioprobes. *Science* **329**, 831-834 (2010).